Topological transitions by magnetization rotation in kagome monolayers of the ferromagnetic Weyl semimetal Co-based shandite

Kazuki Nakazawa [1,2,*] Yasuyuki Kato [1,3] and Yukitoshi Motome [1]

[1]*Department of Applied Physics, The University of Tokyo, Bunkyo, Tokyo 113-8656, Japan*

[2]*RIKEN Center for Emergent Matter Science (CEMS), Wako, Saitama 351-0198, Japan*

[3]*Department of Applied Physics, University of Fukui, Fukui 910-8507, Japan*

(Received 25 February 2024; revised 8 July 2024; accepted 15 July 2024; published 6 August 2024)

Co-based shandite $Co_3Sn_2S_2$ is a ferromagnet hosting Weyl fermions in the layered Co kagome structure. The band topology as well as the magnetism is predicted to vary drastically in the atomically thin films depending on the thickness and surface termination, and as an extreme case, the quantum anomalous Hall state is expected in a monolayer of the Co kagome lattice. Given that the bulk Weyl gap depends on the magnetization direction, here we theoretically study how the topological nature and transport properties vary with the magnetization direction in the systems with kagome monolayer, with both Sn and S surface terminations. By using *ab initio* calculations, we find that in the Sn-end monolayer the anomalous Hall conductivity shows successive discrete changes between different quantized values by rotating the magnetization, indicating several topological transitions between the anomalous quantum Hall insulators with different Chern numbers. Notably, when the magnetization is oriented in-plane and perpendicular to the Co-Co bond, the system exhibits a planar quantum anomalous Hall effect. We clarify that these peculiar behaviors are due to topological changes in the band structures associated with gap closing of the Weyl nodes. In contrast, the S-end monolayer shows rather continuous changes in the transport properties since the system is metallic, although the band structure contains many Weyl nodes. Our results pave the way for controlling Weyl fermions in atomically thin films of Co-based shandite, where the topological nature associated with the Weyl nodes appears more clearly than the bulk.

DOI: 10.1103/PhysRevB.110.085112

I. INTRODUCTION

The Weyl fermion was predicted as a massless elementary particle, which has not yet been found in nature. In condensed matter physics, however, Weyl fermions can appear as quasiparticles in particular crossing points of the electronic band structure, called Weyl nodes [1]. The Weyl nodes always appear in pairs and are regarded as emergent monopoles and antimonopoles in momentum space, which can be characterized by chirality $+1$ and -1, respectively [2]. Their topological properties result in the so-called Fermi arcs on particular surfaces of the system as a consequence of the bulk-edge correspondence [3], and unconventional electromagnetic phenomena, such as the anomalous Hall effect [3–5], the anomalous Nernst effect [6], and the negative magnetoresistance [4,7,8]. A pair of Weyl nodes is generated from a Dirac node by lifting the spin degeneracy, as found in several materials with spatial-inversion symmetry breaking [9–13] or time-reversal symmetry breaking [5,6,14–16].

The Co-based shandite $Co_3Sn_2S_2$, which has stacked kagome planes composed of Co ions [Figs. 1(a) and 1(b)], has attracted attention as a candidate for ferromagnetic Weyl semimetal with Weyl nodes associated with spontaneous breaking of time-reversal symmetry [17,18]. Indeed, this material exhibits giant anomalous Hall and Nernst effects, large negative magnetoresistance [17–21], and surface Fermi arcs [22]. Subsequently, it was proposed that a thin film with Co kagome monolayer of this material realizes a Chern insulator with the quantum anomalous Hall effect [23], which has stimulated the fabrication of atomically thin films [24–28]. Furthermore, it was theoretically revealed that the electronic and magnetic states, band topology, and transport properties vary significantly depending on the number of kagome layers and the surface termination in thin films [29].

In the bulk case, $Co_3Sn_2S_2$ exhibits the ferromagnetic moment perpendicular to the kagome plane [17,18]. A theoretical study based on an effective model showed that the Weyl nodes form nodal rings when the magnetization is oriented in-plane [30]. Furthermore, a previous *ab initio* study demonstrated that the positions of the Weyl nodes in the energy-momentum space can be tuned by controlling the direction of the magnetic moment [31]. The magnetization angle dependence of the anomalous Hall effect as well as the spin Hall effect was also predicted for the effective model [32]. These results indicate that the band topology in this bulk material is sensitive to the magnetization direction. Given that the thin films of this material show a variety of the electronic and magnetic properties as mentioned above, it is interesting to clarify how these properties vary with the magnetization direction in the thin film case. It would be important not only for further understanding the relation between the magnetism and the band topology but also for further stimulating the experiments on thin film fabrication.

In this paper, we study the electronic band structure and transport properties based on the *ab initio* calculations for the

*Contact author: kazuki.nakazawa@riken.jp

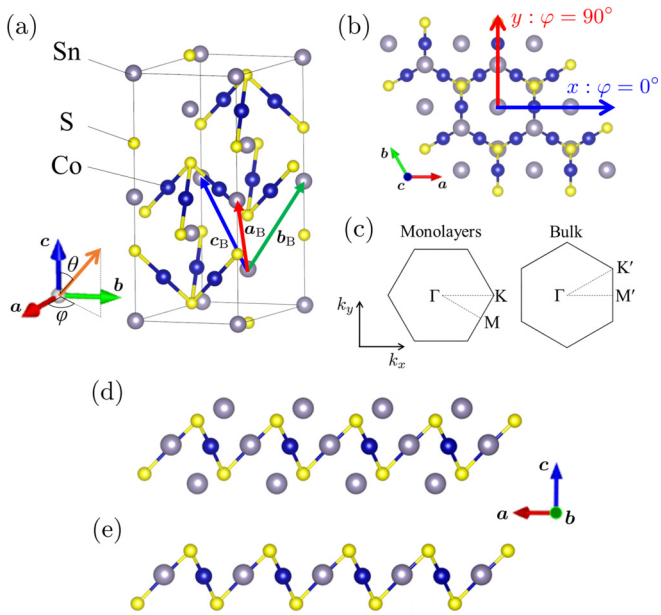

FIG. 1. (a) Lattice structure of the bulk $Co_3Sn_2S_2$. The black box represents the conventional unit cell containing three primitive unit cells. The inset shows the definitions of the polar and azimuthal angles, θ and φ, respectively, which specify the direction of magnetization, with respect to the lattice vectors $\boldsymbol{a}$, $\boldsymbol{b}$, and $\boldsymbol{c}$. $\boldsymbol{a}_B$, $\boldsymbol{b}_B$, and $\boldsymbol{c}_B$ are the primitive vectors for the bulk system. (b) Top view of the Co kagome plane. The directions of $\varphi = 0°$ and $90°$ are indicated; the former (latter) is parallel (perpendicular) to a Co-Co bond. (c) Two-dimensional Brillouin zone for monolayers (left). The cut of the three-dimensional Brillouin zone for the bulk at $k_z = 0$ is also shown (right). [(d) and (e)] Side view of the (d) Sn-end monolayer and (e) S-end monolayer. The crystal structures are visualized by VESTA [33].

thin films with kagome monolayer of the Co-based shandite while changing the direction of the ferromagnetic moment. We consider two types of monolayers with Sn and S surface terminations, following the previous studies [23,29]. We find that the anomalous Hall conductivity σ_H, as well as the anomalous Nernst conductivity α_N, exhibits significantly different behaviors from the bulk system for the magnetization rotation. In particular, in the monolayer with Sn termination, we find that σ_H shows several discrete changes between different quantized values, suggesting topological transitions between the quantum anomalous Hall insulators with different Chern numbers. Interestingly, when the magnetization is oriented in-plane and perpendicular to the Co-Co bond, σ_H is nonzero at a quantized value, indicating a planar quantum anomalous Hall effect. In contrast, in the monolayer with S termination, σ_H shows more moderate changes without showing quantization. We explain these contrasting behaviors depending on the tilted direction of the magnetization and the surface termination by the analyses of the band structure and the Berry phase as well as the symmetry argument.

This paper is organized as follows. After describing the details of *ab initio* calculations and the computations of transport properties in Sec. II, we show the magnetization angle dependences of σ_H and α_N in Sec. III. To understand the results, we discuss the electronic band structure and the Berry curvature in Sec. IV, and also present the symmetry argument in Sec. V. Finally, Sec. VI is devoted to the summary.

II. METHOD

The optimized lattice structures and electronic properties are computed using the OpenMX code [34,35] within the framework of the density functional theory. The Perdew-Burke-Ernzerhof (PBE) generalized gradient approximation (GGA) [36] is employed for the exchange-correlation functional. We consider two types of thin films, each including a Co kagome monolayer with different surface terminations: One has Sn atoms at both surfaces [Fig. 1(d)], while the other has S atoms [Fig. 1(e)]. We call the former and latter the Sn-end and S-end monolayer, respectively. For these monolayers, we employ the set of lattice vectors $\boldsymbol{a}$ and $\boldsymbol{b}$ indicated in the inset of Fig. 1(b), while we use the primitive vectors $\boldsymbol{a}_B$, $\boldsymbol{b}_B$, and $\boldsymbol{c}_B$ in Fig. 1(a) for the bulk calculations. Following the previous study [29], we perform the structural optimization for the monolayers, starting from the lattice structures taken from the bulk and assuming a spin-polarized state within the nonrelativistic calculations. After the optimization, we symmetrize the structure to retain the original $p\bar{3}m1$ symmetry. In the bulk calculations, we use the experimental lattice structures [37].

To study the electronic states while changing the directions of the ferromagnetic moment, we adopt the fully relativistic calculation with a constraint functional $E_{cs} = v\sum_i \mathrm{Tr}[(N_i - N_i^{(0)})^2]$, where N_i and $N_i^{(0)}$ are the occupation matrices consisting of two component spinors at a certain self-consistent field loop and the target spin state, respectively [34]. Here, i is the label of atomic site and we take $v = 5$ meV. We vary the moment direction by changing the polar angle θ from $0°$ to $180°$ for the azimuth angle $\varphi = 0°$ and $\varphi = 90°$; see the inset of Figs. 1(a) and 1(b). Note that the cases of $\theta = 0°$ and $180°$ correspond to the out-of-plane moments, and that the case of $\theta = 90°$ for $\varphi = 0°$ ($90°$) corresponds to the in-plane moment parallel (perpendicular) to a Co-Co bond in the kagome plane. Note also that the resultant moments are roughly oriented in the direction of the constraint, but not perfectly. Such slight tilting leads to small deviations from the results expected from the symmetry, as will be discussed in Sec. V. We take the in-plane direction with $\varphi = 0°$ ($90°$) as the x (y) axis.

To investigate the band topology and the transport properties, we construct tight-binding models from the maximally localized Wannier functions [38,39], which are obtained by OpenMX [40], to reproduce the electronic band structure for each tilting angle of the ferromagnetic moment. Following the previous study [29], we employ Co $3d$, Sn $5s$ and $5p$, and S $3p$ orbitals. The Berry curvature of the nth band at the momentum $\boldsymbol{k}$ is calculated by

$$\Omega_n(\boldsymbol{k}) = -\sum_{m\neq n} \frac{2\mathrm{Im}[J_{x,nm}J_{y,mn}]}{[E_n(\boldsymbol{k}) - E_m(\boldsymbol{k})]^2}, \tag{1}$$

where m is the band index, $E_n(\boldsymbol{k})$ is the nth eigenvalue of the tight-binding Hamiltonian $H(\boldsymbol{k})$, and $\boldsymbol{J}_{nm} = (J_{x,nm}, J_{y,nm})$ is the current operator defined by

$$\boldsymbol{J}_{nm} = \langle n\boldsymbol{k}|\nabla_{\boldsymbol{k}}H(\boldsymbol{k})|m\boldsymbol{k}\rangle, \tag{2}$$

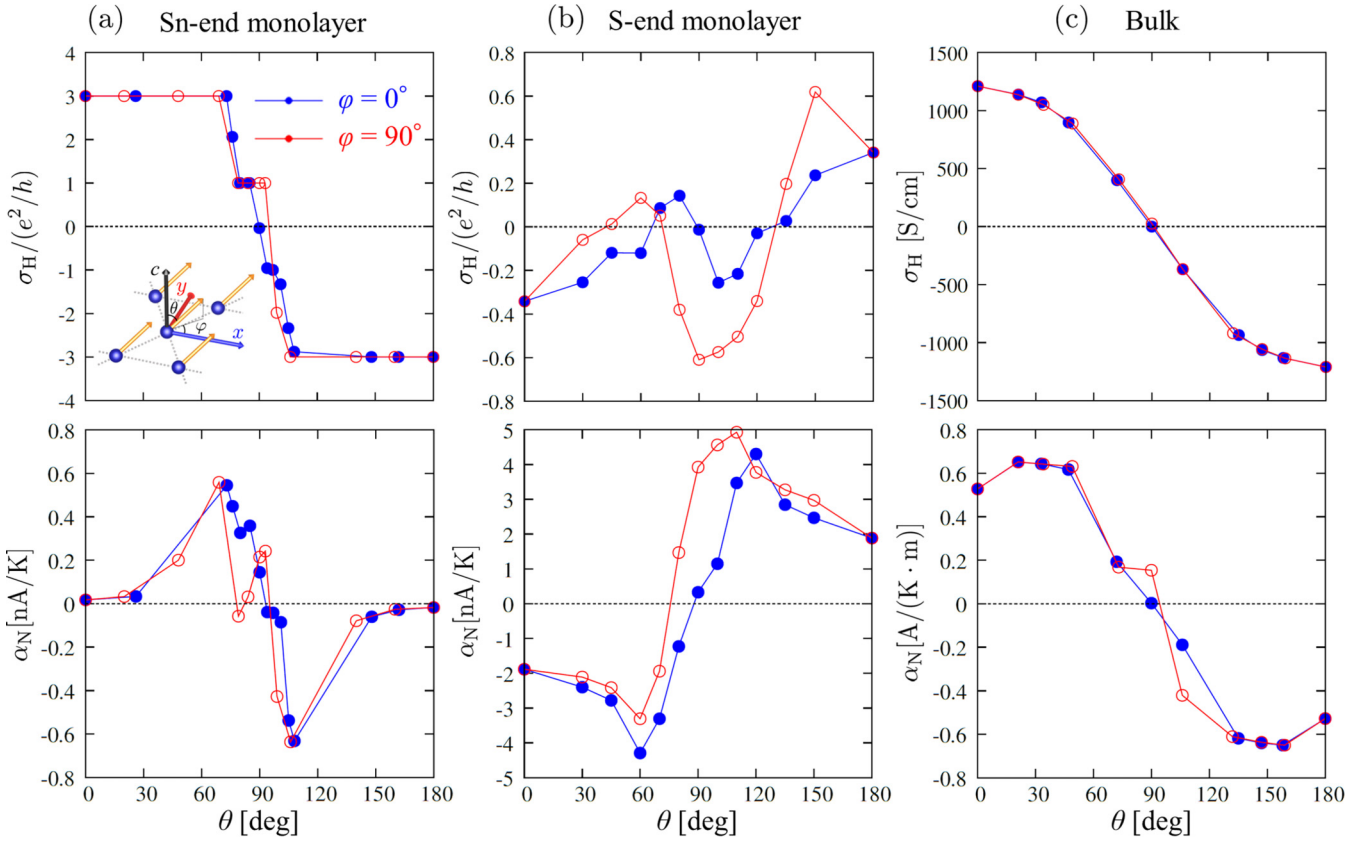

FIG. 2. θ dependences of the anomalous Hall conductivity $\sigma_{\rm H}$ and the anomalous Nernst conductivity $\alpha_{\rm N}$ for (a) the Sn-end monolayer, (b) the S-end monolayer, and (c) the bulk of the Co-based shandite. $\sigma_{\rm H}$ is calculated at zero temperature, while $\alpha_{\rm N}$ is at $k_{\rm B}T = 5$ meV. The blue and red points represent the data for $\varphi = 0^\circ$ and $\varphi = 90^\circ$, respectively. The lines are guide for the eye. The orange arrows in the inset of the upper panel of (a) denote the Co magnetic moments.

with the eigenvector of the Hamiltonian, $|n\boldsymbol{k}\rangle$. The Chern number of the nth band is calculated by

$$C_n = \sum_{\boldsymbol{k}\in \rm BZ} \Omega_n(\boldsymbol{k}), \tag{3}$$

where the sum is taken for the momentum $\boldsymbol{k}$ within the first Brillouin zone [Fig. 1(c)]. Then, based on the Kubo formula, we compute the anomalous Hall conductivity $\sigma_{\rm H}$ and the anomalous Nernst conductivity $\alpha_{\rm N}$ as

$$\sigma_{\rm H} = -\frac{e^2}{\hbar V_d} \sum_{\boldsymbol{k}\in \rm BZ} \sum_n f(E_n(\boldsymbol{k}))\Omega_n(\boldsymbol{k}), \tag{4}$$

$$\alpha_{\rm N} = \frac{ek_{\rm B}}{\hbar V_d} \sum_{\boldsymbol{k}\in \rm BZ} \sum_n s(E_n(\boldsymbol{k}))\Omega_n(\boldsymbol{k}), \tag{5}$$

respectively, where e is the elementary charge, $k_{\rm B}$ is the Boltzmann constant, $\hbar$ is Dirac's constant, and V_d is a d-dimensional volume of the system; $f(\varepsilon) = (\mathrm{e}^{(\varepsilon-\mu)/k_{\rm B}T} + 1)^{-1}$ is the Fermi distribution function, where T and μ are the temperature and the chemical potential, respectively, and $s(\varepsilon)$ is the entropy density given by $s(\varepsilon) = -f(\varepsilon)\ln f(\varepsilon) - [1 - f(\varepsilon)]\ln[1 - f(\varepsilon)]$. In the $\boldsymbol{k}$ summations, the number of the $\boldsymbol{k}$ mesh in the first Brillouin zone is taken as 2000×2000 for monolayers and $480\times480\times480$ for bulk.

III. MAGNETIZATION ANGLE DEPENDENCE OF TRANSPORT PROPERTIES

In this section, we discuss the magnetization angle dependences of $\sigma_{\rm H}$ and $\alpha_{\rm N}$ while tilting the ferromagnetic moment in the $\varphi = 0^\circ$ and $\varphi = 90^\circ$ planes. Figure 2 displays the results for the Sn-end and S-end monolayers as well as the bulk. Here, $\sigma_{\rm H}$ is calculated at absolute zero temperature, while $\alpha_{\rm N}$ is obtained at $k_{\rm B}T = 5$ meV.

Let us first focus on the Sn-end monolayer [Fig. 2(a)]. In both cases of $\varphi = 0^\circ$ and 90°, $\sigma_{\rm H}$ exhibits discrete stepwise changes for θ. For $\varphi = 0^\circ$, $\sigma_{\rm H}$ changes between integer values in unit of e^2/h: $+3$, $+1$, -1, and -3, where h is Planck's constant. This behavior indicates that the system undergoes successive topological transitions between the quantum anomalous Hall insulating states with nonzero Chern numbers $C = -3$, -1, $+1$, and $+3$. We can confirm this by the plateaulike features in the chemical potential dependence of $\sigma_{\rm H}$; see Appendix A. In this case, $\sigma_{\rm H}$ as well as $\alpha_{\rm N}$ shows almost antisymmetric dependence on θ with respect to $\theta = 90^\circ$, indicating that the topologically trivial state with $C = 0$ is realized for the in-plane magnetization with $\theta = 90^\circ$. In contrast, in the case of $\varphi = 90^\circ$, both $\sigma_{\rm H}$ and $\alpha_{\rm N}$ are no longer antisymmetric. In particular, $\sigma_{\rm H}$ shows stepwise changes from $+3$ to $+1$ and to -3 in units of e^2/h, without taking -1, indicating that the system undergoes different sequences of topological transitions from the case of $\varphi = 0^\circ$. Strikingly, $\sigma_{\rm H}$

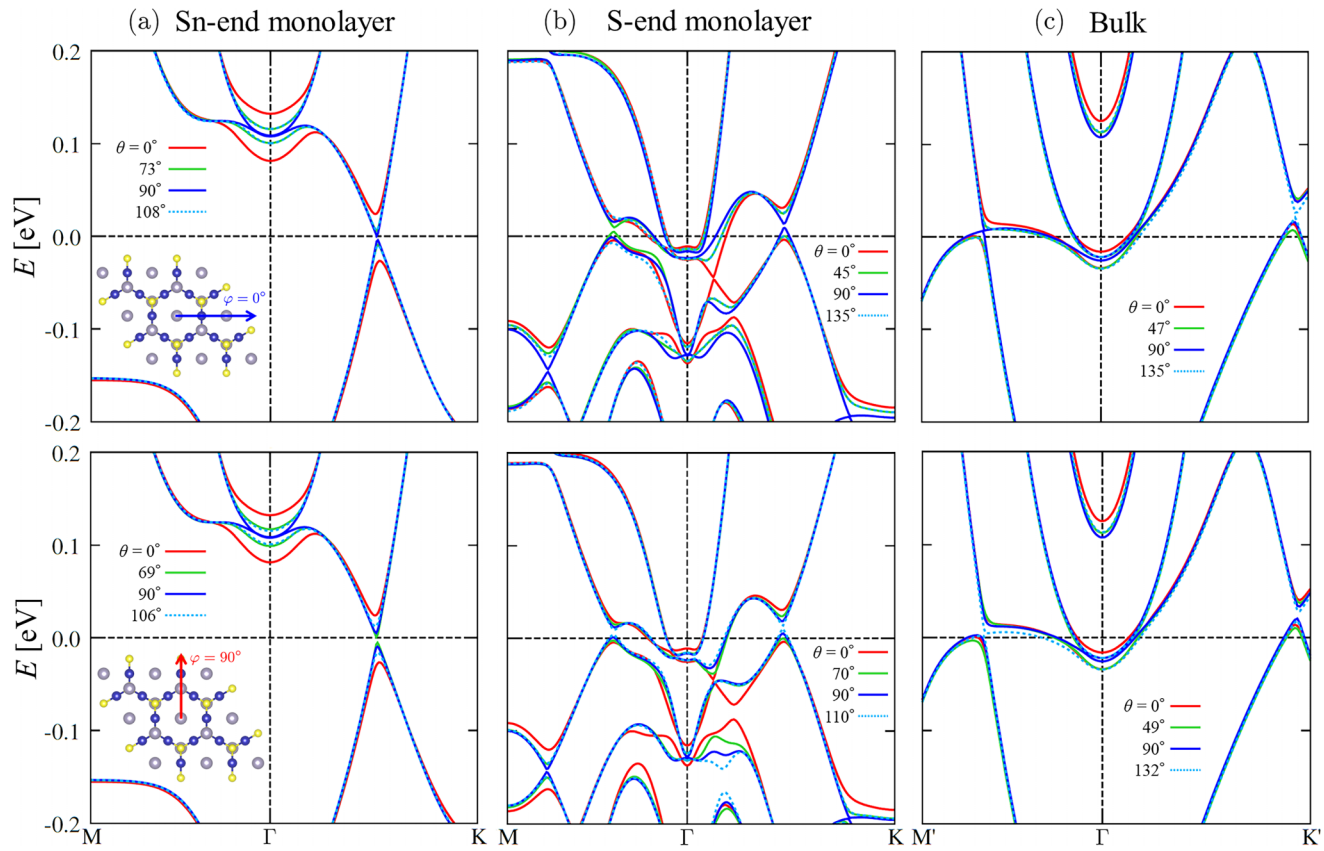

FIG. 3. Electronic band structures near the Fermi level ($E = 0$) of (a) the Sn-end monolayer, (b) the S-end monolayer, and (c) the bulk for selected values of the tilting angle θ. The upper and lower panels show the results for $\varphi = 0°$ and $\varphi = 90°$ cases, respectively. M(M′), Γ, and K(K′) are the symmetric points defined in Fig. 1(c).

is quantized at $+1$ even for the in-plane magnetization with $\theta = 90°$, suggesting a planar quantum anomalous Hall effect [41–44]. The contrasting behaviors between $\varphi = 0°$ and $90°$ will be discussed from the symmetry point of view in Sec. V.

Next, we discuss the results for the S-end monolayer [Fig. 2(b)]. In this case, σ_H is no longer quantized at any nonzero integer values and shows rather continuous changes with θ for both $\varphi = 0°$ and $90°$. This is because the system is always metallic, as will be shown in Sec. IV. The complicated θ dependences with sign changes are ascribed to the changes of the band structure with several Weyl nodes. We note that the θ dependences of σ_H and α_N are again almost antisymmetric with respect to $\theta = 90°$ for $\varphi = 0°$, while they are not for $\varphi = 90°$, similar to the Sn-end case in Fig. 2(a).

For comparison, we also study the bulk case [Fig. 2(c)]. We observe rather smooth and monotonic θ dependences of σ_H and α_N compared with the monolayers. These behaviors are qualitatively consistent with the previous studies [30–32]. Also in this bulk case, σ_H and α_N are almost antisymmetric for $\varphi = 0°$, but not for $\varphi = 90°$ [32]. The deviation is larger in α_N because it is related to the energy derivative of σ_H through the generalized Mott's relation [45], and thus detects the asymmetry rather sensitively.

Consequently, our results highlight the distinctive transport behaviors while changing the magnetization direction in the monolayer systems. In particular, the Sn-end monolayer exhibits successive discrete changes of σ_H, indicating topological transitions between different anomalous quantum Hall insulators. In addition, this behavior appears differently for $\varphi = 0°$ and $90°$, suggesting that the topological transitions take place in a different manner depending on the tilting direction. These findings will be discussed from the viewpoints of the electronic band structure and the Berry curvature in the next section.

IV. ELECTRONIC BAND STRUCTURE AND BERRY CURVATURE

In this section, we present the electronic band structures obtained by the *ab initio* calculations, and discuss the relation between their magnetization angle dependences and the results in the previous section. Figure 3 shows the electronic band structures along the symmetric lines in the Brillouin zones shown in Fig. 1(c) near the Fermi level set at zero while changing the tilting angle θ for (a) the Sn-end monolayer, (b) the S-end monolayer, and (c) the bulk. The upper and lower panels display the results for $\varphi = 0°$ and $\varphi = 90°$, respectively.

We first discuss the case of Sn-end monolayer [Fig. 3(a)]. In this case, the magnitude of magnetic moment is almost independent of θ, $\sim 1\ \mu_B$ per formula unit [23,29]. The magnetic anisotropy between out-of-plane and in-plane ferromagnetic states is estimated as ~ 1 meV per formula unit [29], which corresponds to the Zeeman field of ~ 6 T. The band structure

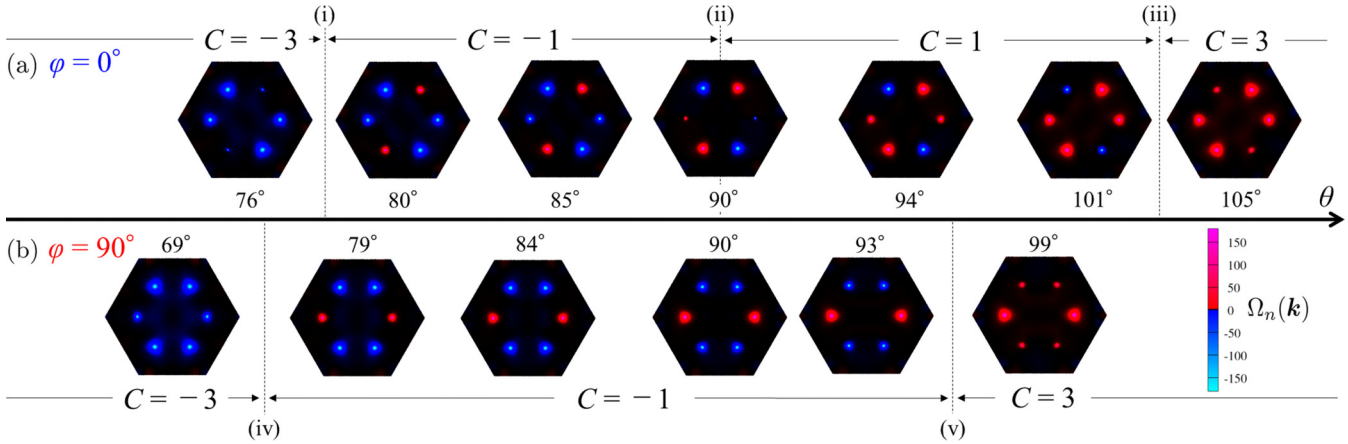

FIG. 4. θ dependences of the Berry curvature $\Omega_n(\boldsymbol{k})$ in the first Brillouin zone of the band just below the Fermi level for the Sn-end monolayer: (a) $\varphi = 0^\circ$ and (b) $\varphi = 90^\circ$. The changes of the Chern number C are also indicated. (i)–(v) represent the topological transitions associated with the changes of C. The band index n for the Chern number is dropped.

around the Weyl gap is dominated by majority spin state, similar to the bulk system. The system at $\theta = 0^\circ$, namely, with the out-of-plane magnetic moment, is an anomalous quantum Hall insulator with the Chern number $C = -3$ with the Weyl gap opening along the Γ-K line [23,29]. While tilting the moment by increasing θ, the Weyl gap decreases and closes around $\theta = 90^\circ$ for $\varphi = 0^\circ$, as shown in the upper panel of Fig. 3(a); see also Appendix B. In this case, the change of the band structure is almost antisymmetric with respect to $\theta = 90^\circ$; for instance, the results for $\theta = 73^\circ$ and $\theta = 108^\circ$ are almost equivalent. Meanwhile, for $\varphi = 90^\circ$, the Weyl gap similarly decreases and closes around $\theta = 69^\circ$ as shown in the lower panel of Fig. 3(a) [46].

In Fig. 4, we show the magnetization angle dependence of the Berry curvature of the band just below the Fermi level in the Sn-end monolayer. We present the Berry curvature of the other bands near the Fermi level in Appendix B. In the case of $\varphi = 0^\circ$ [Fig. 4(a)], we find that the sign reversal of the Berry curvature associated with the Weyl gap closing occurs (i) between $\theta = 76^\circ$ and $\theta = 80^\circ$, (ii) at $\theta = 90^\circ$, (iii) between $\theta = 101^\circ$ and $\theta = 105^\circ$. These correspond to the topological transitions inferred by $\sigma_{\rm H}$ in Fig. 2(a) with the changes of the Chern number as (i) $C = -3 \to -1$, (ii) $C = -1 \to +1$ via $C = 0$ at $\theta = 90^\circ$, and (iii) $C = 1 \to 3$. We note that the Berry curvature along the $k_x = 0$ axis remains at $\theta = 90^\circ$ since the very small Weyl gap remains due to small local in-plane spin canting presumably coming from the Dzyaloshinskii-Moriya type mechanism [47]; the gap should be closed if the magnetic moments are perfectly parallel to the a axis; see the symmetry argument in Sec. V. In contrast, in the case of $\varphi = 90^\circ$ [Fig. 4(b)], there are two topological transitions (iv) between $\theta = 69^\circ$ and $\theta = 79^\circ$ and (v) between $\theta = 93^\circ$ and $\theta = 99^\circ$, where the Chern number changes as $C = -3 \to -1$ and $-1 \to 3$, respectively. These correspond well to the θ dependence of $\sigma_{\rm H}$ in Fig. 2(a). The θ evolution of the Berry curvature is asymmetric with respect to $\theta = 90^\circ$, and the number of topological transitions is one less than in $\varphi = 0^\circ$, because the two pairs of Weyl gaps close simultaneously at the transition (v). The asymmetric change leaves the nonzero Chern number at $\theta = 90^\circ$ (see also Appendix B), which leads to the planar quantum anomalous Hall effect discussed in Sec. III.

Next, we discuss the results for the S-end monolayer [Fig. 3(b)]. In this case, the magnitude of the magnetization is around $\sim 3\ \mu_{\rm B}$ per formula unit [23,29], which is again almost independent of θ. The magnetic anisotropy between out-of-plane and in-plane states is ~ 0.03 meV [29], corresponding to the Zeeman field of ~ 0.17 T, which is smaller than the Sn-end case. The band structure around the Fermi level contains both majority and minority spin states in contrast to the Sn-end case as well as the bulk case, and is always metallic for both $\varphi = 0^\circ$ and 90°, which prevents $\sigma_{\rm H}$ from being quantized as found in Fig. 2(b). Furthermore, there are a greater number of gapped Weyl nodes at low energy than the Sn-end monolayer; see also Appendix B. These Weyl gaps close and cause topological transitions at various magnetization angles, leading to the complicated θ dependences in Fig. 2(b). Nevertheless, for $\varphi = 0^\circ$, the band structure changes almost antisymmetric with respect to $\theta = 90^\circ$, as represented by almost the same band structures for $\theta = 45^\circ$ and $\theta = 135^\circ$. This is consistent with almost antisymmetric behavior of $\sigma_{\rm H}$ and $\alpha_{\rm N}$ in Fig. 2(b), similar to the Sn-end case.

Finally, we briefly discuss the bulk result [Fig. 3(c)]. The system is always metallic, similar to the S-end monolayer case. Besides, the band structure around the Fermi level is much simpler and the number of Weyl gaps are more scarce than the S-end monolayer, leading to the simpler θ dependences of $\sigma_{\rm H}$ and $\alpha_{\rm N}$. We observe the gap closing on the M′-Γ line at $\theta = 90^\circ$ and the Γ-K′ line at $\theta = 135^\circ$ in the $\varphi = 0^\circ$ case, and the M′-Γ line at $\theta = 132^\circ$ in the $\varphi = 90^\circ$ case.

V. SYMMETRY ARGUMENT

Let us discuss the band topology from the symmetry point of view. As mentioned in Sec. II, the lattice structures of the monolayers are symmetrized after the optimization, which have threefold rotational symmetry around the c axis, C_{3c}, twofold rotational symmetry around the a axis, C_{2x}, the mirror symmetry perpendicular to the a axis, M_x, and the spatial inversion symmetry $C_{2x}M_x$.

We first focus on the $\varphi = 0^\circ$ case. When $\theta = 90^\circ$ where all the magnetic moments are perfectly oriented along the a axis

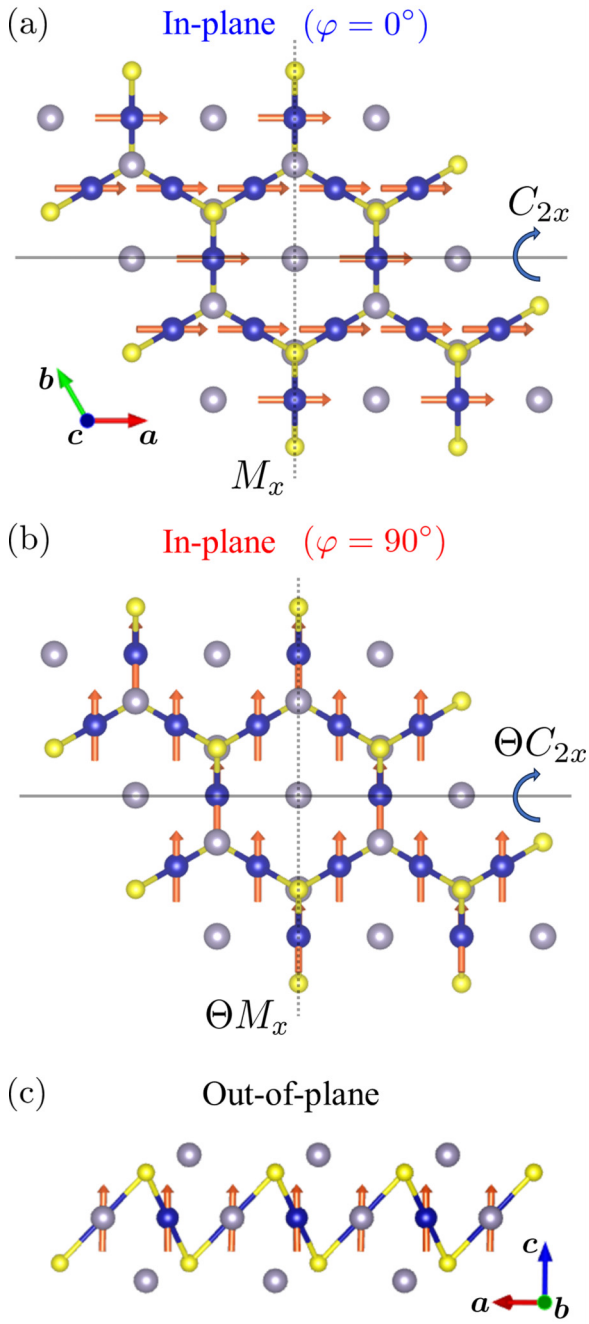

FIG. 5. Schematic pictures of (a) the in-plane ($\varphi = 0°$), (b) in-plane ($\varphi = 90°$), and (c) out-of-plane directions of the ferromagnetic moments, which are parallel to $\boldsymbol{a}$, $\boldsymbol{c}\times\boldsymbol{a}$, and $\boldsymbol{c}$, respectively. The orange arrows represent the Co magnetic moments. The relevant symmetries to our analysis are denoted in (a) and (b).

[Fig. 5(a)], C_{2x} and M_x symmetries are preserved. Hence, in this case, the Berry curvature should satisfy the relations

$$\Omega(k_x, -k_y)|_{\theta=90°,\varphi=0°} = -\Omega(k_x, k_y)|_{\theta=90°,\varphi=0°}, \quad (6)$$

$$\Omega(-k_x, k_y)|_{\theta=90°,\varphi=0°} = -\Omega(k_x, k_y)|_{\theta=90°,\varphi=0°}. \quad (7)$$

Note that the band index n for the Berry curvature is dropped here and hereafter. These lead to the cancellation of the Berry curvature in each band, and consequently, the disappearance of the anomalous Hall and Nernst conductivities. In particular, these relations indicate $\Omega(k_x, 0) = \Omega(0, k_y) = 0$, meaning that the Berry curvature vanishes on the k_x and k_y axes. These arguments are indeed approximately satisfied in the *ab initio* results in the previous sections. Note that in this case the out-of-plane component of a net magnetization is prohibited because of C_{2x} and M_x symmetry.

We can extend the argument to general θ. Since the state with $\theta = 90° - \gamma$ and $\theta = 90° + \gamma$ are related with each other via the C_{2x} or M_x operation, we obtain the relations

$$\Omega(k_x, -k_y)|_{\theta=90°-\gamma,\varphi=0°} = -\Omega(k_x, k_y)|_{\theta=90°+\gamma,\varphi=0°}, \quad (8)$$

$$\Omega(-k_x, k_y)|_{\theta=90°-\gamma,\varphi=0°} = -\Omega(k_x, k_y)|_{\theta=90°+\gamma,\varphi=0°}. \quad (9)$$

These are consistent with the results in Fig. 4(a). Equations (8) and (9) lead to the relations of $\sigma_{\rm H}$ and $\alpha_{\rm N}$ as

$$\sigma_{\rm H}|_{\theta=90°-\gamma,\varphi=0°} = -\sigma_{\rm H}|_{\theta=90°+\gamma,\varphi=0°}, \quad (10)$$

$$\alpha_{\rm N}|_{\theta=90°-\gamma,\varphi=0°} = -\alpha_{\rm N}|_{\theta=90°+\gamma,\varphi=0°}, \quad (11)$$

respectively. These explain well our *ab initio* results in Fig. 2.

Next we consider the case of $\varphi = 90°$. In Fig. 5(b), we illustrate the situation of in-plane ferromagnetic state with $\theta = 90°$ as a typical example. In this case, the system remains invariant under the ΘC_{2x} and ΘM_x operations, where Θ is a time-reversal operator. This is because the magnetic moment is parallel to the mirror plane. We note that the out-of-plane component of a net magnetization is allowed from the symmetry, while we obtained negligibly small net moment from our *ab initio* calculation without energy constraint. Since the same argument can be made for general θ, the Berry curvature should satisfy the relations

$$\Omega(k_x, -k_y)|_{\varphi=90°} = \Omega(k_x, k_y)|_{\varphi=90°}, \quad (12)$$

$$\Omega(-k_x, k_y)|_{\varphi=90°} = \Omega(k_x, k_y)|_{\varphi=90°}, \quad (13)$$

for all θ. These are consistent with the *ab initio*-based analysis shown in Fig. 4(b) and allow the appearance of the anomalous Hall and Nernst effects [31], including the planar quantum anomalous Hall effect found in Fig. 2(a).

From the above discussion, we can predict the behavior of transport properties when the magnetization is rotated in the kagome plane ($\theta = 90°$). Since $\sigma_{\rm H} = 0$ when $\varphi = 0°$, it should vanish when $\varphi = (60n)°$ (n is an integer). Similarly, $\sigma_{\rm H}/(e^2/h) = \pm 1$ when $\varphi = (\mp 30 + 120n)°$. Thus, when the magnetization is rotated in the kagome plane, $\sigma_{\rm H}$ changes as $0 \to +1 \to 0 \to -1 \to 0 \cdots$ in unit of e^2/h with 120° period.

Finally, we comment on the case of out-of-plane moment [Fig. 5(c)]. In this case, Eqs. (8) and (9) with $\gamma = 90°$ give the relations between the two cases of out-of-plane moments, $\theta = 0°$ and $\theta = 180°$. In addition, Eqs. (12) and (13) hold. These relations are again consistent with the results in the previous sections.

VI. SUMMARY

To summarize, focusing on the thin films of Co-based shandite with Co kagome monolayer, we have investigated

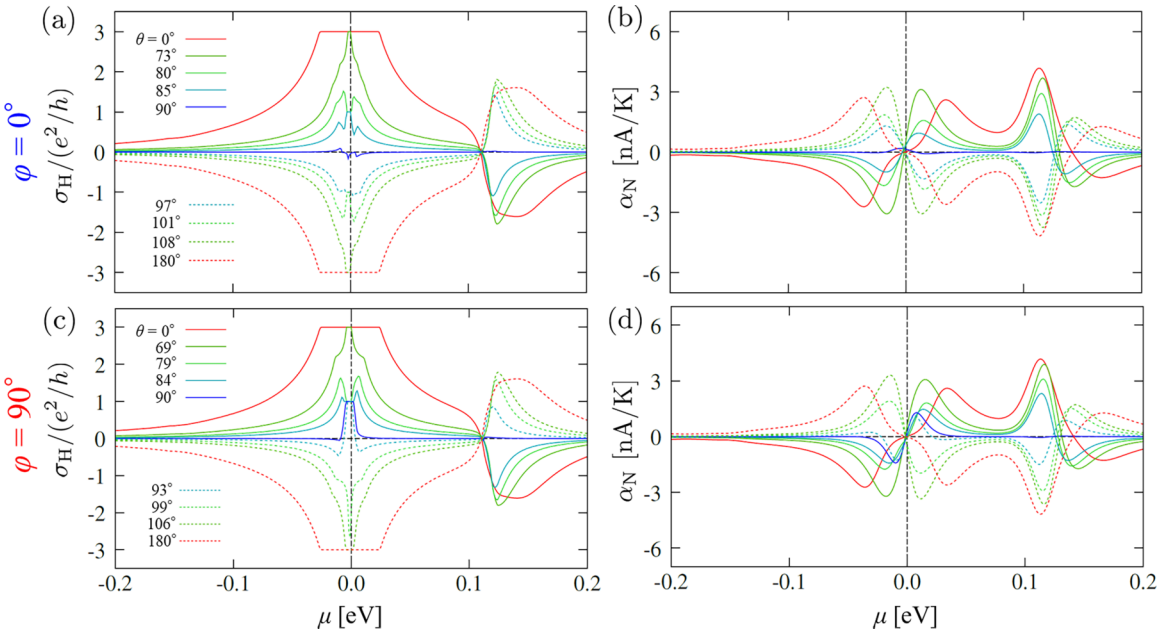

FIG. 6. Chemical potential dependences of [(a) and (c)] the anomalous Hall conductivity σ_H at zero temperature and [(b) and (d)] the anomalous Nernst conductivity α_N at the temperature of 5 meV in the Sn-end monolayer. The data are calculated for $\varphi = 0^\circ$ in (a) and (b), and for $\varphi = 90^\circ$ in (c) and (d), at several tilting angles θ.

the magnetization angle dependences of the electronic state, band topology, and transport properties. Using the *ab initio* calculations, we revealed distinctive behaviors depending on the surface termination of the films. In the Sn-end monolayer, we found successive topological phase transitions between the Chern insulating states with different Chern numbers while rotating the magnetization direction, resulting in discrete changes in the anomalous Hall conductivity σ_H between the corresponding quantized values. Remarkably, we discovered the planar quantum anomalous Hall effect: σ_H is quantized with nonzero Chern number even when the magnetization is oriented in the in-plane direction perpendicular to a Co-Co bond. In contrast, in the S-end monolayer, σ_H as well as the anomalous Nernst conductivity α_N shows moderate changes without quantization as the system is always metallic. We show the origins of these behaviors by careful analyses of the Berry curvature distributions in each band and the symmetry arguments. Our results pave the way for controlling topological properties of the Weyl semimetal toward device applications, by leveraging various tuning methods for the magnetic anisotropy in thin films, such as magnetostriction, substrate effects, and thickness changes.

ACKNOWLEDGMENTS

The authors thank K. Fujiwara, K. Kobayashi, K. Nomura, S. Okumura, A. Ozawa, and A. Tsukazaki for fruitful discussions. This work is supported by JST CREST (Grant No. JPMJCR18T2) and JSPS KAKENHI (Grants No. JP21K13875 and No. JP22K03509).

APPENDIX A: CHEMICAL-POTENTIAL DEPENDENCES OF TRANSPORT PROPERTIES IN THE SN-END MONOLAYER

In this Appendix, we present the chemical potential dependences of the anomalous Hall conductivity σ_H and the anomalous Nernst conductivity α_N for the Sn-end monolayer. Figure 6 shows the results calculated for the band structures at several values of θ, by changing the chemical potential in Eqs. (4) and (5). As discussed in Secs. III and IV, the Sn-end monolayer is in the Chern insulating states with different quantized values of σ_H depending on the moment direction. Correspondingly, we find integer plateaus around zero chemical potential: $\sigma_H/(e^2/h) = +3$, $+1$, -1, and -3 for $\varphi = 0^\circ$ [Fig. 6(a)], and $\sigma_H/(e^2/h) = +3$, $+1$, and -3 for $\varphi = 90^\circ$ [Fig. 6(c)]. These plateaus represent the Weyl gaps which make the system being the Chern insulators. In addition, in the case of $\varphi = 0^\circ$, we confirm that the relations in Eqs. (10) and (11) are approximately satisfied at all values of the chemical potential. We also note that α_N shown in Figs. 6(b) and 6(d) are approximately given by the chemical potential derivative of σ_H, as expected from the generalized Mott relation [45].

APPENDIX B: BERRY CURVATURE IN EACH BAND

In this Appendix, we show the Berry curvature in each band for Sn-end and S-end monolayers as well as the bulk. Figures 7(a), 7(d), and 7(g) show that the Sn-end monolayer is in the distinct Chern insulating states for the out-of-plane, in-plane ($\varphi = 0^\circ$), and in-plane ($\varphi = 90^\circ$) moments, respectively. We can also observe that the gap is almost closed on the k_x and k_y axes in the in-plane x case from Fig. 7(d). Note that

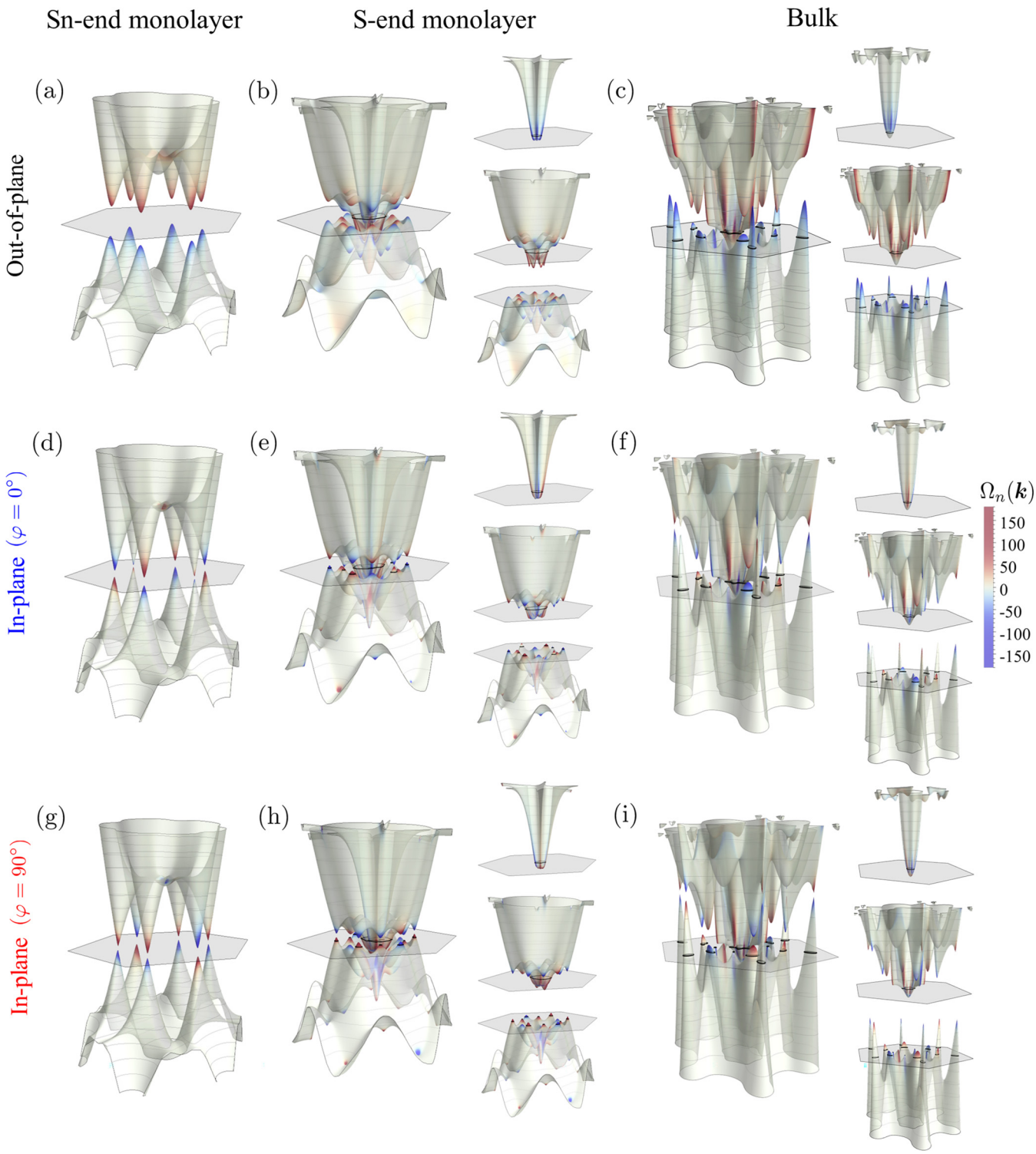

FIG. 7. Berry curvature with the band structure of [(a), (d), (g)] Sn-end monolayer, [(b), (e), (h)] S-end monolayer, and [(c), (f), (i)] $k_z = 0$ cut of bulk for the [(a)–(c)] out-of-plane, [(d)–(f)] in-plane ($\varphi = 0°$), and [(g)–(i)] in-plane ($\varphi = 90°$) magnetic moments in the energy range from -0.2 eV to 0.2 eV. The black lines on the gray hexagons in each panel represent the Fermi surfaces. The small panels in the row of S-end monolayer and bulk present the results in each band separately.

the Berry curvatures at $\theta = 90°$ shown in Fig. 4 correspond to the results in the lower band depicted in Figs. 7(d) and 7(g). In the S-end cases shown in Figs. 7(b), 7(e), and 7(h), the distribution of the Weyl nodes where the Berry curvature becomes intense is complicated as discussed in Secs. III and IV. Figures 7(c), 7(f), and 7(i) are the similar plots for the bulk in the $k_z = 0$ cut, again showing the consistency with the symmetry arguments.

[1] N. P. Armitage, E. J. Mele, and A. Vishwanath, Weyl and Dirac semimetals in three-dimensional solids, Rev. Mod. Phys. **90**, 015001 (2018).

[2] H. B. Nielsen and M. Ninomiya, The Adler-Bell-Jackiw anomaly and Weyl fermions in a crystal, Phys. Lett. B **130**, 389 (1983).

[3] S. Murakami, Phase transition between the quantum spin Hall and insulator phases in 3D: Emergence of a topological gapless phase, New J. Phys. **9**, 356 (2007).

[4] A. A. Burkov, Chiral anomaly and transport in Weyl metals, J. Phys.: Condens. Matter **27**, 113201 (2015).

[5] T. Suzuki, R. Chisnell, A. Devarakonda, Y.-T. Liu, W. Feng, D. Xiao, J. W. Lynn, and J. G. Checkelsky, Large anomalous Hall effect in a half-Heusler antiferromagnet, Nat. Phys. **12**, 1119 (2016).

[6] A. Sakai, Y. P. Mizuta, A. A. Nugroho, R. Sihombing, T. Koretsune, M. Suzuki, N. Takemori, R. Ishii, D. Nishio-Hamane, R. Arita, P. Goswami, and S. Nakatsuji, Giant anomalous Nernst effect and quantum-critical scaling in a ferromagnetic semimetal, Nat. Phys. **14**, 1119 (2018).

[7] X. Huang, L. Zhao, Y. Long, P. Wang, D. Chen, Z. Yang, H. Liang, M. Xue, H. Weng, Z. Fang, X. Dai, and G. Chen, Observation of the chiral-anomaly-induced negative magnetoresistance in 3D Weyl semimetal TaAs, Phys. Rev. X **5**, 031023 (2015).

[8] C.-L. Zhang, S.-Y. Xu, I. Belopolski, Z. Yuan, Z. Lin, B. Tong, G. Bian, N. Alidoust, C.-C. Lee, S.-M. Huang, T.-R. Chang, G. Chang, C.-H. Hsu, H.-T. Jeng, M. Neupane, D. S. Sanchez, H. Zheng, J. Wang, H. Lin, C. Zhang *et al.*, Signatures of the Adler–Bell–Jackiw chiral anomaly in a Weyl fermion semimetal, Nat. Commun. **7**, 10735 (2016).

[9] S.-Y. Xu, I. Belopolski, N. Alidoust, M. Neupane, G. Bian, C. Zhang, R. Sankar, G. Chang, Z. Yuan, C.-C. Lee, S.-M. Huang, H. Zheng, J. Ma, D. S. Sanchez, B. Wang, A. Bansil, F. Chou, P. P. Shibayev, H. Lin, S. Jia *et al.*, Discovery of a Weyl fermion semimetal and topological Fermi arcs, Science **349**, 613 (2015).

[10] S. Souma, Z. Wang, H. Kotaka, T. Sato, K. Nakayama, Y. Tanaka, H. Kimizuka, T. Takahashi, K. Yamauchi, T. Oguchi, K. Segawa, and Y. Ando, Direct observation of nonequivalent Fermi-arc states of opposite surfaces in the noncentrosymmetric Weyl semimetal NbP, Phys. Rev. B **93**, 161112(R) (2016).

[11] H. Weng, C. Fang, Z. Fang, B. A. Bernevig, and X. Dai, Weyl semimetal phase in noncentrosymmetric transition-metal monophosphides, Phys. Rev. X **5**, 011029 (2015).

[12] A. A. Soluyanov, D. Gresch, Z. Wang, Q.-S. Wu, M. Troyer, X. Dai, and B. A. Bernevig, Type-II Weyl semimetals, Nature (London) **527**, 495 (2015).

[13] B. Feng, Y.-H. Chan, Y. Feng, R.-Y. Liu, M.-Y. Chou, K. Kuroda, K. Yaji, A. Harasawa, P. Moras, A. Barinov, W. Malaeb, C. Bareille, T. Kondo, S. Shin, F. Komori, T.-C. Chiang, Y. Shi, and I. Matsuda, Spin texture in type-II Weyl semimetal WTe_2, Phys. Rev. B **94**, 195134 (2016).

[14] X. G. Wan, A. M. Turner, A. Vishwanath, and S. Y. Savrasov, Topological semimetal and Fermi-arc surface states in the electronic structure of pyrochlore iridates, Phys. Rev. B **83**, 205101 (2011).

[15] G. Xu, H. Weng, Z. Wang, X. Dai, and Z. Fang, Chern semimetal and the quantized anomalous Hall effect in $HgCr_2Se_4$, Phys. Rev. Lett. **107**, 186806 (2011).

[16] J. Kübler and C. Felser, Weyl points in the ferromagnetic Heusler compound Co_2MnAl, Europhys. Lett. **114**, 47005 (2016).

[17] Q. Wang, Y. Xu, R. Lou, Z. Liu, M. Li, Y. Huang, D. Shen, H. Weng, S. Wang, and H. Lei, Large intrinsic anomalous Hall effect in half-metallic ferromagnet $Co_3Sn_2S_2$ with magnetic Weyl fermions, Nat. Commun. **9**, 3681 (2018).

[18] E. Liu, Y. Sun, N. Kumar, L. Muechler, A. Sun, L. Jiao, S.-Y. Yang, D. Liu, A. Liang, Q. Xu, J. Kroder, V. Süß, H. Borrmann, C. Shekhar, Z. Wang, C. Xi, W. Wang, W. Schnelle, S. Wirth, Y. Chen *et al.*, Giant anomalous Hall effect in a ferromagnetic kagome-lattice semimetal, Nat. Phys. **14**, 1125 (2018).

[19] S. N. Guin, P. Vir, Y. Zhang, N. Kumar, S. J. Watzman, C. Fu, E. Liu, K. Manna, W. Schnelle, J. Gooth, C. Shekhar, Y. Sun, and C. Felser, Zero-field nernst effect in a ferromagnetic kagome-lattice Weyl-semimetal $Co_3Sn_2S_2$, Adv. Mater. **31**, 1806622 (2019).

[20] H. Yang, W. You, J. Wang, J. Huang, C. Xi, X. Xu, C. Cao, M. Tian, Z.-A. Xu, J. Dai, and Y. Li, Giant anomalous nernst effect in the magnetic Weyl semimetal $Co_3Sn_2S_2$, Phys. Rev. Mater. **4**, 024202 (2020).

[21] Y. Yanagi, J. Ikeda, K. Fujiwara, K. Nomura, A. Tsukazaki, and M. T. Suzuki, First-principles investigation of magnetic and transport properties in hole-doped shandite compounds $Co_3In_xSn_{2-x}S_2$, Phys. Rev. B **103**, 205112 (2021).

[22] D. F. Liu, Q. N. Xu, E. K. Liu, J. L. Shen, C. C. Le, Y. W. Li, D. Pei, A. J. Liang, P. Dudin, T. K. Kim, C. Cacho, Y. F. Xu, Y. Sun, L. X. Yang, Z. K. Liu, C. Felser, S. S. P. Parkin, and Y. L. Chen, Topological phase transition in a magnetic Weyl semimetal, Phys. Rev. B **104**, 205140 (2021).

[23] L. Muechler, E. Liu, J. Gayles, Q. Xu, C. Felser, and Y. Sun, Emerging chiral edge states from the confinement of a magnetic Weyl semimetal in $Co_3Sn_2S_2$, Phys. Rev. B **101**, 115106 (2020).

[24] K. Fujiwara, J. Ikeda, J. Shiogai, T. Seki, K. Takanashi, and A. Tsukazaki, Ferromagnetic $Co_3Sn_2S_2$ thin films fabricated by co-sputtering, Jpn. J. Appl. Phys. **58**, 050912 (2019).

[25] J. Shiogai, J. Ikeda, K. Fujiwara, T. Seki, K. Takanashi, and A. Tsukazaki, Robust perpendicular magnetic anisotropy of $Co_3Sn_2S_2$ phase in sulfur deficient sputtered thin films, Phys. Rev. Mater. **5**, 024403 (2021).

[26] J. Ikeda, K. Fujiwara, J. Shiogai, T. Seki, K. Nomura, K. Takanashi, and A. Tsukazaki, Critical thickness for the emergence of Weyl features in $Co_3Sn_2S_2$ thin films, Commun. Mater. **2**, 18 (2021).

[27] J. Ikeda, K. Fujiwara, J. Shiogai, T. Seki, K. Nomura, K. Takanashi, and A. Tsukazaki, Two-dimensionality of metallic surface conduction in $Co_3Sn_2S_2$ thin films, Commun. Phys. **4**, 117 (2021).

[28] K. Fujiwara, J. Ikeda, S. Ito, and A. Tsukazaki, Electrochemical thinning of Co kagome-lattice layers in ferromagnetic $Co_3Sn_2S_2$ thin films by bias-induced Co dissolution, J. Appl. Phys. **133**, 125302 (2023).

[29] K. Nakazawa, Y. Kato, and Y. Motome, Magnetic, transport and topological properties of Co-based shandite thin films, Commun. Phys. **7**, 48 (2024).

[30] A. Ozawa and K. Nomura, Two-orbital effective model for magnetic Weyl semimetal in kagome-lattice shandite, J. Phys. Soc. Jpn. **88**, 123703 (2019).

[31] M. P. Ghimire, J. I. Facio, J.-S. You, L. Ye, J. G. Checkelsky, S. Fang, E. Kaxiras, M. Richter, and J. van den Brink, Creating Weyl nodes and controlling their energy by magnetization rotation, Phys. Rev. Res. **1**, 032044(R) (2019).

[32] A. Ozawa, K. Kobayashi, and K. Nomura, Effective model analysis of intrinsic spin Hall effect with magnetism in the stacked kagome Weyl semimetal $Co_3Sn_2S_2$, Phys. Rev. Appl. **21**, 014041 (2024).

[33] K. Momma and F. Izumi, VESTA 3 for three-dimensional visualization of crystal, volumetric and morphology data, J. Appl. Cryst. **44**, 1272 (2011).

[34] http://www.openmx-square.org.

[35] T. Ozaki, Variationally optimized atomic orbitals for large-scale electronic structures, Phys. Rev. B **67**, 155108 (2003).

[36] J. P. Perdew, K. Burke, and M. Ernzerhof, Generalized gradient approximation made simple, Phys. Rev. Lett. **77**, 3865 (1996).

[37] G. Li, Q. Xu, W. Shi, C. Fu, L. Jiao, M. E. Kamminga, M. Yu, H. Tüysüz, N. Kumar, V. Süß, R. Saha, A. K. Srivastava, S. Wirth, G. Auffermann, J. Gooth, S. Parkin, Y. Sun, E. Liu, and C. Felser, Surface states in bulk single crystal of topological semimetal $Co_3Sn_2S_2$ toward water oxidation, Sci. Adv. **5**, eaaw9867 (2019).

[38] N. Marzari and D. Vanderbilt, Maximally localized generalized Wannier functions for composite energy bands, Phys. Rev. B **56**, 12847 (1997).

[39] I. Souza, N. Marzari, and D. Vanderbilt, Maximally localized Wannier functions for entangled energy bands, Phys. Rev. B **65**, 035109 (2001).

[40] H. Weng, T. Ozaki, and K. Terakura, Revisiting magnetic coupling in transition-metal-benzene complexes with maximally localized Wannier functions, Phys. Rev. B **79**, 235118 (2009).

[41] X. Liu, H.-C. Hsu, and C.-X. Liu, In-plane magnetization-induced quantum anomalous Hall effect, Phys. Rev. Lett. **111**, 086802 (2013).

[42] Y. Ren, J. Zeng, X. Deng, F. Yang, H. Pan, and Z. Qiao, Quantum anomalous Hall effect in atomic crystal layers from in-plane magnetization, Phys. Rev. B **94**, 085411 (2016).

[43] P. Zhong, Y. Ren, Y. Han, L. Zhang, and Z. Qiao, In-plane magnetization-induced quantum anomalous Hall effect in atomic crystals of group-V elements, Phys. Rev. B **96**, 241103(R) (2017).

[44] Z. Liu, G. Zhao, B. Liu, Z. F. Wang, J. Yang, and F. Liu, Intrinsic quantum anomalous Hall effect with in-plane magnetization: Searching rule and material prediction, Phys. Rev. Lett. **121**, 246401 (2018).

[45] D. Xiao, Y. Yao, Z. Fang, and Q. Niu, Berry-phase effect in anomalous thermoelectric transport, Phys. Rev. Lett. **97**, 026603 (2006).

[46] For $\varphi = 0^\circ$, the Weyl gaps on the other symmetric lines close around $\theta = 76^\circ$ and $\theta = 105^\circ$. Meanwhile, for $\varphi = 90^\circ$, the Weyl gaps on the other two symmetric lines close simultaneously around $\theta = 99^\circ$. See Fig. 4.

[47] I. V. Solovyev, Linear response theories for interatomic exchange interactions, J. Phys.: Condens. Matter **36**, 223001 (2024).